Journal of Materials Chemistry A

Single-Crystal Based Studies for Correlating Properties and High-Voltage Performance of Li[NixMnyCo1-x-y]O2 Cathodes

Journal:	*Journal of Materials Chemistry A*
Manuscript ID	TA-ART-10-2018-010329.R1
Article Type:	Paper
Date Submitted by the Author:	01-Feb-2019
Complete List of Authors:	Zhu, Jian; Lawrence Berkeley National Laboratory, ESDR Chen, Guoying; Lawrence Berkeley National Laboratory, EETD

Single-Crystal Based Studies for Correlating Properties and High-Voltage Performance of $Li[Ni_xMn_yCo_{1-x-y}]O_2$ Cathodes

Jian Zhu[a] and Guoying Chen[a,] *

[a.] *Energy Storage and Distributed Resources Division, Lawrence Berkeley National Laboratory, Berkeley, California 94720, USA*

* *Corresponding author's email:* gchen@lbl.gov

Abstract

Safe and stable cycling of lithium-ion battery cathodes at high voltages is essential for meeting the next-generation energy storage demands, yet the lack of fundamental understanding of material's properties and reactivities correlation largely hinders current progress. In the present study, we show how single-crystal samples with well-controlled physical characteristics can be used to unambiguously establish the relationships among specific properties, surface chemistry and electrochemical performance, enabling rational design of better performing cathode materials. Layered $Li[Ni_xMn_yCo_{1-x-y}]O_2$ (NMC) crystals, with four different particle shapes of octahedron (Oct), truncated octahedron (T-Oct), polyhedron (Poly) and platelet (Plate), were prepared to vary the presence of (104), (001) and (012) family facets on the surface. This represents the first experimental verification on NMC morphologies that were theoretically calculated in the past. Systematic studies on the impact of isolated physical properties reveal the important roles of Ni content, particle size and facet on surface stability and electrochemical performance. We show that compared to (012) surface dominated samples, high-voltage cycling stability was much improved on the (001) dominated Plate sample, suggesting that replacing (012) surface with lower energy

(001) and/or (104) surface can be effective in stabilizing NMCs during high energy applications. Our study further provides insights on how tailoring material's surface properties can be used as an important route in balancing cathode capacity and stability.

1. Introduction

Lithium-ion batteries (LIBs) have been the dominant power sources for portable electronics for decades and are now the mainstream energy storage choice for the electric vehicle markets. With the relatively high capacity and high operating voltage, nickel-rich layered transition metal oxides with a general formula of $Li[Ni_xMn_yCo_{1-x-y}]O_2$ ($x \geq 0.5$, Ni-rich NMCs) are considered most promising for high-energy LIBs in large-scale applications.[1-6] However, the poor high-voltage cycling stability of these oxide cathodes limits their commercial adopation.[7-8] Currently, there is an urgent need for fundamental understanding of degradation mechanism and factors that control the degradation, especially at high voltages. Such knowledge is critical in order to design future generation of NMC materials with better performance and stability.[9-12]

Several processes are known to affect the stability of NMCs when cycled to high voltages, including: 1) structural transformation from layered to spinel and/or rock-salt phases,[13-16] 2) mechanical damage such as crack formation in active particles,[17-18] 3) parasitic reactions between cathode and the electrolyte,[19-21] and 4) migration, segregation and dissolution of transition metals (TMs).[22-25] Physical characteristics of primary particles, such as composition, size and morphology, can be expected to play a large role in each of these processes. Previous studies using density functional theory (DFT) calculations revealed the importance of primary particle surface on cathode reactivity and cycling stability.[26-29] For example, the calculation carried out on $LiCoO_2$ and NMC111 determined that their equilibrium particle shapes are consisting of (104), (001) and (012) facets,[26-27] and the (104) family facets are more stable than (012) facets during electrochemical cycling. Experimentally, oxygen release and thermal decomposition of $LiCoO_2$ were found to be facet-dependent, and structural reconstruction from the layered to spinel and rock-salt phases occurred preferably on (012) and (104) family facets, as opposed to the (001)

facets.[30] Ni and Co segregation were also found on selective surfaces of layered oxides cathode materials ($R\bar{3}m$ space group).[31] Recently, intra-granular cracking resulting from high-voltage cycling of the layered oxides was found to progress from the grain interior along the (003) planes, which led to bulk structural degradation and reduced long-term stability.[18, 32]

In conventional NMC samples, the large porous aggregates of secondary particles consist of various sized primary particles. Naturally, material performance is controlled by the physical properties of primary particles as well as the properties of the secondary particles, such as particle size distribution, porosity, grain boundaries, etc. It is difficult to isolate the impact of a specific material's property in these studies, which hinders systematic investigation on the influence of NMC composition, primary particle size and shape/surface facets on their electrochemical performance and stability. Nonetheless, obtaining these understanding is essential for material design and optimization as well as correlating with theory efforts on material behavior. Herein, we explore different approaches to synthesize NMC single-crystal samples with a variety of compositions, sizes and morphologies. For the first time, we prepare NMC single crystals with two different types of dominating surfaces, providing experimental verification to the theoretically calculated morphology. We further use this family of samples to correlate the impact of specific physical attribute on material properties and behavior. Our study provides much needed insights for rational design of layered cathode materials with improved performance and stability.

2. Experimental Section

2.1. Synthesis

NMC single-crystal samples were prepared *via* a molten-salt method or a co-precipitation followed by annealing process. In the typical molten-salt synthesis, stochiometric amounts of $Ni(NO_3)_2 \cdot 6H_2O$, $Mn(NO_3)_2 \cdot 4H_2O$ and $Co(NO_3)_2 \cdot 6H_2O$ (Sigma-Aldrich, > 99%) were dissolved in a trace amount of distilled water which then thoroughly mixed with a Li precursor (10-30 mol.% in excess). The use of extra lithium precursor was necessary for compensating Li loss typically experienced during high temperature heating. A flux was then added to the mixture at a specified molar ratio between the flux and the TM precursors (denoted as R ratio hereafter). The mixture was further ground for 30 min, heated at 200 ºC for 3 h and 850 ºC for 10 h at a ramping rate of 4 ºC/min, and then cooled to room temperature naturally. The final NMC products were collected by dissolving KCl in distilled water, filtrating and thorough washing with distilled water. To obtain single-crystal samples with different sizes and morphologies, a combination of various TM and Li precursors, flux, R ratio and annealing conditions were used. In a typical coprecipitation-annealing method, the stoichiometric amount of metal sulfates and 0.5 g polyvinylpyrrolidone (PVP, average M_w =1,300,000 determined by the light scattering curve) were dissolved in distilled water to obtain a mixed metal sulfate solution. A NaOH/ammonia (2M/0.2M) aqueous solution was prepared and then added dropwise to a 1M ammonia aqueous solution under stirring, along with the metal sulfate solution. The pH of the mixture was maintained at 11-12 for 20 h. The precipitate from the reaction was filtered and washed with distilled water several times to remove dissolved salts. The as-obtained transition metal hydroxides precursor was dried in a vacuum oven at 60 ºC overnight, mixed with $LiOH \cdot H_2O$ (6 mol.% excess) and annealed at 850 ºC for 10 h to obtain the final NMC product.

2.2. Characterization

Powder X-ray diffraction (PXRD) was carried out using Bruker D2 powder X-ray diffractometer (λ (Cu K_α) = 0.15418 nm, 40 kV, 30 mA). The morphology of NMC sample was characterized using JEOL JSM-7500F field emission scanning electron microscope (SEM) at an accelerating voltage of 15 kV. The powder samples were sputtered with a thin layer of Au before the analysis to improve conduction. Chemical composition analysis was carried out using inductively coupled plasma-optical emission spectrometry (ICP-OES. Perkin-Elmer Optima 5300 DV). Hard X-ray absorption spectroscopy (hXAS) spectra of Ni, Mn and Co *K*-edge were collected in transmission mode using a (220) monochromator at Stanford Synchrotron Radiation Light source (SSRL) beamline 2-2. NMC powder samples were sealed between two pieces of Kapton tapes for data collection. Si (220) monochromator was re-detuned for each element before the measurement to reduce the higher harmonics in the X-ray beam. Energy calibration was carried out by setting the first inflection points in the spectra of Ni, Mn and Co metal foil references to be 8333 eV, 6539 eV, and 7709 eV respectively. X-ray absorption near edge structure (XANES) spectra were processed using SIXPACK software. Soft XAS (sXAS) spectra were collected at SSRL on the 31-pole wiggler beamline 10-1 in a single load at ambient temperature under ultra-high vacuum (10^{-9} Torr), using the total electron yield (TEY) and fluorescence yield (FY) mode detectors. A ring current of 350 mA, a 1000 l mm^{-1} spherical grating monochromator with 40 μm entrance and exit slits, a 0.2 eV energy resolution and a 1 mm^2 beam spot were used. A thin layer of powder sample was loaded onto conductive carbon tape on aluminum sample holder inside argon-filled glovebox for sXAS measurement. sXAS spectra data was processed using the PyMca software.

2.3. Electrochemistry

To prepare the composite electrode, the as-prepared NMC crystals, a poly (vinylidene fluoride) (PVDF) binder and acetylene black conductive additive were mixed in N-methylpyrrolidone (NMP) solvent in a weight ratio of 8:1:1. The slurry was then coated onto a carbon-coated aluminum foil current collector (Exopack Advanced Coatings) and dried at 120 ºC in a vacuum oven for overnight. NMC composite electrodes with an area of 1.6 cm^2 and an active mass loading of ~3 mg/cm^2 were then cut from the coated Al sheets. Half-cells were assembled in 2032-type coin cells in an argon-filled glovebox (O_2 < 1 ppm and H_2O < 1 ppm), using Li foil (Alfa-Aesar) as the counter and reference electrodes, NMC composite electrode as the working electrode, Celgard 2325 membrane as separator in a GEN 2 electrolyte (1.2 M $LiPF_6$ in ethylene carbonate (EC)/ethyl methyl carbonate (EMC) 3:7, Novolyte Technologies Inc.). The electrochemical performance was evaluated at ambient temperature on a VMP3 multichannel potentiostat/galvanostat controlled by EC-lab software (BioLogic Science Instruments).

3. Results and discussion

3.1. Synthesis of NMC single-crystal samples

Previously, DFT calculations reported that the equilibrium shapes of layered NMC particles are enclosed by three families of facets, namely (104), (001), and (012).[26] Among them, the surface energy of (012) and (104) are the highest and lowest, respectively, suggesting they are the least and most thermodynamically favorable surface. Our recent theory-based studies showed that surface fraction of each facet can be influenced by the chemical potentials of oxygen and lithium during synthesis. At lower oxygen chemical potential conditions, such as in a less oxidizing atmosphere or at a lower reaction temperature, (104) appears in favor over (012) on the surface. On the other hand, (001) facets are more sensitive to lithium chemical potential, whose surface

presence increases with decreasing lithium chemical potential. Figure 1 is a schematic showing the possible equilibrium shapes of single crystal NMC enclosed by (012), (001) and/or (104). The *x*-axis is the shape evolution as a function of O chemical potential which influences (104) presence. The *y*-axis shows the evolution as a function of Li chemical potential which influences (001) presence. Enclosed in the dashed box are possible shapes with all three families of facets. Thermodynamically, the (012)-enclosed rhombohedron has the highest surface energy and is therefore least stable under equilibrium conditions. Upon reducing O or Li chemical potential, NMC particles may evolve into more stable morphology by diminishing the proportion of high-energy (012) facets on the surface. Experimentally, synthesis conditions that lead to the formation of particles with only one or two facet families are likely stringent or nonexistent. The possible equilibrium crystalline shapes enclosed by all three facets are shown in Figure 1 inset, namely (012) dominating truncated octahedron and polyhedron, (104) dominating tetradecahedron, and (001) dominating platelet.

Based on these understanding, synthesis methods and synthesis parameters were explored to obtain NMC single crystals with varying sizes and morphologies. Figure 2 shows the SEM images of typical NMC samples prepared in this study. We obtained the octahedron-shaped (Oct, Figure 2a), truncated-octahedron-shaped (T-oct, Figure 2b) and polyhedron-shaped (Poly, Figure 2c) crystal samples by using a molten-salt method where the transition-metal and Li precursors reacted at an elevated temperature in the presence of a molten flux. For the Oct sample, a mixture of CsCl and LiCl (1:4) was used as the flux for the reaction between the transition-metal acetates and Li_2CO_3 at 900 ^oC. T-Oct samples were prepared by mixing TM nitrates, lithium hydroxide or lithium carbonate in a KCl flux at an R ratio between 4 and 48. The typical temperature was in the range of 850 to 900 ^oC. To obtain the Poly samples, a mixture of TM nitrates, lithium nitrate and

CsCl flux were used. The R ratio was reduced to 2 and heating time was reduced to 8 h. The typical temperature used was 850 ^{o}C. Although the exact O potential for each synthesis condition is difficult to determine, the trend appears to follow the theoretical prediction that a reduction in oxygen chemical potential leads to enhanced (104) presence on the surface. For example, the Poly sample, which had the highest (104) fraction, was obtained using a lower reaction temperature and shorter reaction time. The platelet-shaped sample (Plate, Figure 2d) was prepared *via* a coprecipitation-annealing method. The TM hydroxide precursor was first prepared in an aqueous solution containing TM sulfates, NaOH and ammonia. The as-obtained hydroxide was then mixed with LiOH and annealed at 850 or 800 ^{o}C to obtain the NMC Plate sample. Detailed synthesis conditions for obtaining each crystal sample are also summarized in Table 1. Figure S1 shows the XRD patterns collected on the different morphologies. Hexagonal α-$NaFeO_2$ type structure with an $R\bar{3}m$ space group was confirmed for all samples. Analysis on XRD peak intensity confirms the nature of anisotropic crystal growth. For example, the (012)/(003) and (104)/(003) intensity ratios on the Plate sample are 0.17 and 0.75, respectively, while they are around 0.1 and 0.4-0.5 on Oct, T-Oct, and Poly samples. The larger ratios on the Plates are consistent with the preferred growth direction along <012> and <104> relative to <003>, which results in the dominating (001) surface. The similarity in the XRD patterns of Oct, T-Oct, and Poly samples are likely due to the same dominating (012) surface on all three samples.

The single-crystal nature of NMC samples prepared using the same procedure was investigated in a previous publication.[33] Particles were surveyed by SAED to verify single crystalline orientation throughout the particle. In this study, shape analysis was used to index the planes and also quantify their relative percentage on the surface. Based on the SEM image shown in Figure 2, crystal shapes of each sample were built and analyzed by using VESTA (JP-Minerals),

a 3D visualization program for structural models. While the surfaces on Oct, T-Oct and Poly samples were dominated by (012) facets, the presence of (104) facet gradually increased with the increasing of truncation. More specifically, while the Oct crystals were enclosed by 88% of (012) facets and 12% percent of (001), T-Oct crystals had 85% of (012), 10% of (001) and 5% of (104) facets. For the Poly sample, the percentage changed to 70%, 5% and 25% for (012), (001) and (104), respectively. The most significant difference between the Plate and the Oct/T-Oct/Poly sample series lies in the ratio between (001) and (012) facets as more than 85% of the Plate surface is covered by the (001) facets (Figure 3).

NMC single-crystal samples with size ranging from 10 μm to 0.1 μm were also prepared. For simplicity, only the synthesis of T-Oct NMC532 is discussed here, although other compositions were also made under similar conditions. We found that the size of T-Oct shaped single crystals is most sensitive to the type and amount of the flux as well as the annealing conditions used during the synthesis. In general, crystal size decreases with the increasing R ratio between the flux and the TM precursors. Particles larger than 0.5 μm were obtained by using a small amount of CsCl or KCl flux ($R \leq 4$), whereas those below 0.5 μm can be prepared by using a large amount of KCl flux (R=48). Figure 4 shows the SEM images of obtained T-Oct NMC532 crystals with varying particle sizes.

The above synthesis approaches are mostly applicable for preparing NMC crystal samples with different compositions and a series of morphology- and size-controlled NMC333, NMC532, NMC622 and NMC811 were synthesized. The chemical compositions of the samples were analyzed and verified by ICP analysis, and the results are summarized in Table S1. The large library of samples allowed us to investigate the role of specific oxide property while maintaining all others the same within the series. In the following sections, we discuss in detail the impact of

Ni content, particle size and surface facets on NMC structure, chemical properties and cathode performance and stability.

3.2 Impact of NMC Ni content

To investigate the role of Ni content, we focused on a series of NMC crystal samples with three different compositions of 333, 622 and 811, all with the same size of 1 μm, same shape of truncated-octahedron and dominating (012) surface, and the same Mn/Co ratio. Figure 5a shows the XRD patterns of the samples, with the inset showing the atomic structure of layered NMC. In the typical hexagonal α-$NaFeO_2$ type structure with an $R\bar{3}m$ space group, lithium cations occupy the octahedral 3*b* sites and TM (Ni, Mn and Co in this case) cations co-occupy the octahedral 3*a* sites to form the transition-metal layer. Peak splitting in (006)/(012) and (018)/(110) doublets is typically observed,[34] which is often used as an indicator for structural ordering in the hexagonal crystal structure. The presence of peak splitting in the XRD patterns collected on all three samples confirms the formation of layered structure. With the increase of Ni content, the splitting gradually narrowed, which suggests a reduction in the layering quality. This is consistent with the increasing cation mixing resulting from the size similarity between Ni^{2+} (0.69 Å) and Li^+ (0.76 Å), as reported in previous studies.[35] The enhanced cation mixing in NMC811 is also evidenced by the decreased intensity ratio of I(003)/I(104) on the XRD pattern.

Rietveld refinement of the XRD patterns collected on NMC333, NMC622 and NMC811 T-Oct samples were carried out and the results are shown in Figure S2. The *a* and *c* lattice parameters for NMC333, NMC622 and NMC811 were 2.8646(1) and 14.2336(1) Å, 2.8752(1) and 14.2339(4) Å, and 2.8883(4) and 14.251(2) Å, respectively. These values are similar to what

was reported in the literature.[12, 36-41] With increasing Ni content, the smaller Co^{3+} (0.545 Å) and Mn^{4+} (0.53 Å) are replaced by larger-sized Ni cation, either Ni^{2+} (0.69 Å) or Ni^{3+} (0.60 Å), which leads to an overall increase in the lattice dimension. The *c*/*a* ratio, on the other hand, decreased from 4.97 in NMC333 to 4.93 in NMC811, further confirming reduced quality in layered structure due to increased Ni/Li cation mixing.

Synchrotron soft XAS with depth profiling capability was used to probe the chemical changes on the surface and in the surface-bulk region. By using TEY and FY detectors, TM oxidation states on the top 5 and 50 nm can be evaluated, respectively. Figure 5b shows the Ni L_3-edge spectra collected on NMC333, NMC622 and NMC 811 T-Oct samples. As the intensity ratio between the high energy and low energy L_3 peaks (I_{high}/I_{low}) is often used as an index for the Ni oxidation state,[42-45] we normalized all the spectra to the intensity of the low energy peak. With increasing Ni content, an increase in L_3 high energy peak was observed on both TEY and FY spectra, consistent with the increase of Ni oxidation state in higher Ni content NMCs. The stronger high energy peak in FY mode as compared to that in the TEY mode indicates that surface Ni is at a lower oxidation state, likely a result of surface reduction as observed in previous studies.[43-44] The oxidation state of Mn and Co, however, was not influenced by the Ni content as the L_3-edge sXAS spectra of Mn and Co are nearly identical in all three samples (Figure S3a and S3b). Based on the TM reference spectra (Figure S4), Mn and Co oxidation states were determined to be 4+ and 3+, respectively. The oxidation state of bulk TMs was evaluated by hard XAS and the results on Ni, Mn and Co are shown in Figure 5c, Figure S3c and S3d, respectively. With increasing Ni content, Ni *K*-edge energy, determined by the intensity at 0.5 in the normalized spectrum, gradually shifted towards higher value, consistent with an increase in bulk oxidation state. The Mn and Co *K*-edge spectra in

Figure S3c and S3d further confirm that bulk Mn and Co are at 4+ and 3+, respectively, and their oxidation states are independent of Ni content in the NMC.

Figure 5d compares Ni *K*-edge energy position as well as the intensity ratios of high energy/low energy L_3 peaks as a function of theoretical Ni oxidation state in the NMC. A similar linear relationship was observed on *K*-edge energy and FY *L*-edge intensity ratio, corresponding to the increase of Ni oxidation state from +2 in NMC333 to +2.88 in NMC811 in both bulk and surface-bulk regions. The TEY intensity ratio is generally lower, and the difference becomes more significant as Ni content increases, a result of higher surface reactivity in the presence of Ni^{3+}.

Figure 6 compares the electrochemical performance of the crystals. The samples were made into composite electrodes and cycled in a half cell at a constant rate of C/10 between 3-4.3 V and 3-4.6 V. Because Ni redox occurs at lower potential than that of Co, increasing Ni content in NMC leads to more Li extraction and an increase in the initial discharge capacity in both voltage windows. As expected, initial capacity also increases with increasing upper cutoff voltage from 4.3 to 4.6 V. In both cases, there is an increase in the rate of capacity fade, as shown in the capacity retention plot in Figure 6b. The study demonstrates the intrinsic trade-offs between capacity and the electrochemical stability, in the absence of influence from particle microstructure such as size, morphology and porosity.

3.3. Impact of NMC primary particle size

Figure 7a shows the XRD patterns collected on three NMC532 crystal samples with a particle size of 10 μm, 1 μm and 0.1 μm, respectively, all with the same T-Oct shape and dominating (012) surface. The samples had the well-ordered layered structure with the splitting in

(006)/(012) and (018)/(110) double peaks clearly shown. Results from the Rietveld refinements (Figure S5) showed that *a* and *c* lattice parameters for the 10, 1 and 0.1 μm NMC532 samples were 2.8671(5) and 14.2374(6) Å, 2.8771(1) and 14.2587(8) Å and 2.8765(1) and 14.2578(8) Å, respectively. While the values for the 1 and 0.1 μm samples are consistent with those reported in the literature,[36-41] the slightly reduced lattice dimension in the 10 μm sample may suggest mechanical strain in the much larger NMC particles. The similarity in the *c*/*a* ratio in 0.1 and 1 μm samples further suggests that synthesis parameters are not likely to play a significant role in the layered structure.

Figure 7b shows Ni, Mn and Co TEY L_3-edge soft XAS profiles collected on the three samples. In NMC532, the theoretical oxidation states of Ni, Mn and Co are 2.4+, 4+ and 3+, respectively. When the particle size reduced from 10 to 1 μm, there is a reduction in the intensity ratio between the high energy peak and the low energy peak in the L_3 profile, suggesting lower Ni oxidation state. The ratio in the 1 and 0.1 μm samples, on the other hand, are similar. This is likely a result of increased surface area in smaller particles where more Ni reduction can occur. Compared to the standard spectra shown in Figure S4, the Mn and Co *L*-edge spectra of all three samples suggest their respective oxidation state close to the theoretical values of 4+ and 3+. The bulk oxidation states of the TMs were also evaluated by the hard XAS *K*-edge XANES and the spectra are shown in Figure 7c. These results are consistent with oxidation state of 2.4+, 4+ and 3+ for Ni, Mn and Co, confirming similar bulk chemical properties of the samples.

We further evaluated the electrochemical performance of the samples through galvanostatic cycling (Figure 8a and 8b) and rate capability testing (Figure 8c). The crystals were prepared into composite electrodes and cycled in a half cell at a constant rate of C/10 between 3-4.3 V and 3-4.6 V. As shown in Figure 8a, decreasing particle size increases the initial discharge

capacity in both voltage windows. When cycled to the upper cutoff voltage of 4.3 V, the 1st cycle discharge capacities were 116, 127 and 132 mAh/g for 10, 1 and 0.1 μm samples, respectively. The lower capacity in the 10 μm sample is likely a result of kinetic hindrance and poorer material utilization. As expected, increasing the upper cutoff voltage to 4.6 V increases the initial discharge capacity but at the expense of cycling stability. The 1st cycle discharge capacities were 188, 183 and 191 mAh/g for 10, 1 and 0.1 μm samples, respectively. These similar values suggest that the over-potential at the higher voltage is able to extract more Li and greatly improve the utilization in the large particles. Figure 8b directly compares the particle size effect on the cycling stability in both voltage windows. When cycled between 3 and 4.3 V, the only slightly outperforms 1 and 0.1 μm samples, which had similar performance. With the higher cutoff voltage of 4.6 V, there is an overall decrease in cycling stability as charge/discharge with larger extent of Li involvement naturally destabilized the layered crystal structure. The liquid electrolytes are typically reactive above 4.3 V and side reactions between the cathode and the electrolyte further contributes to the instability. The smaller particles had a larger surface to volume ratio and therefore experienced more severe deterioration due to the side reactions, as compared to the 10 μm sample. We further compare the performance of the samples at C/25, C/10 and C/5 rates, and the results are shown in Figure 8c. At all cycling rates, the 10 and 0.1 μm samples had the lowest and highest discharge capacity, respectively. This is consistent with the observation that larger particles have poorer material utilization due to the longer Li diffusion length.[46]

3.4. Impact of NMC surface facet

To evaluate the impact of surface facet, comparative studies were performed on (001) surface dominated Plate and (012) surface dominated T-Oct NMC333 samples, both with the same

size of 0.1 μm. Figure 9a shows the XRD patterns collected on the samples. The layered crystal structure was obtained, with the clear splitting in (006)/(012) and (018)/(110) peaks confirming low degree of cation mixing in NMC333. Although the structural index on the XRD is the same, the orientation effect is obvious when the peak intensity ratio is analyzed. Smaller (003)/(012) and (003)/(014) peak intensity ratios were observed on the Plate sample, consistent with the slower growth along the <003> direction and a larger presence of (001) on the surface, as compared to that of the (012) surface dominated T-Oct sample.

Comparison of the TEY and FY Ni *L*-edge soft XAS profiles are shown in Figure 9b. The Plate sample experienced less surface Ni reduction than that of the T-Oct sample, as indicated by the higher intensity ratio between the high energy and the low energy peaks. This suggests that the (001) surface with lower surface energy is more resistant to chemical reduction during synthesis and processing. Bulk Ni remains at 2+ in both samples, as shown in Ni *K*-edge hard XAS profiles in Figure 9c. The presence of Mn^{4+} and Co^{3+} in the bulk are also confirmed by Mn and Co *K*-edge hXAS profiles in Figure S6.

Figure 10 compares the cycling performance of the NMC333 samples. When cycled to an upper cutoff voltage of 4.3 V, the initial discharge capacities of the T-Oct and Plate samples were similar at about 125 mA h/g. Increasing the cutoff voltage to 4.6 V leads to an increase in discharge capacity, but the change is more significant for the T-Oct sample which delivered 171 mAh/g, whereas the Plate sample had 157 mAh/g. The difference is likely due to enhanced material utilization driven by the over-potential. NMC333 with the dominating (012) surface benefited more from the driving force than that with the (001) surface, which is impermeable to Li. The increase in initial discharge capacity, however, comes at the expense of the cycling stability, as faster capacity decay is clearly shown in Figure 10b. The results clearly show that surface facet

has significant impact on electrochemical performance at both low and high cutoff voltages. As the (001) surface is parallel to the TM layers, it is Li impermeable.[26-27] On the other hand, (012) surface has efficient Li diffusion pathways. The net result is that particles with large (001) surface tend to have lower utilization and capacity but better stability as compared to the sample with the (012) surface. The higher surface energy of (012) family facets also makes them more reactive and less stable during electrochemical cycling.

4. Conclusions

By using different synthesis approaches and synthesis conditions, a large library of layered NMC single-crystal samples with varying chemical compositions of 333, 532, 622, and 811, varying sizes ranging from 0.1 to 10 μm, and varying morphologies of Oct, T-Oct, Poly and Plate were synthesized. This allows the investigation of the role of specific NMC properties, such as Ni content, size and surface facet, well isolated from the interference from each other as well as other uncontrolled factors. We found that increasing Ni content leads to lower quality layered structure, more severe surface Ni reduction, higher initial capacity but poorer cycling stability. Smaller primary particles experienced enhanced surface TM reduction, a direct result of increased ratio between the surface area and volume. Furthermore, when particle size was reduced, better rate performance was achieved because of the shorter Li diffusion length. Surface facets were found to play a critical role in material stability and cycling performance. The (012) surface is generally more reactive than (001), which is evidenced by enhanced surface Ni reduction, higher initial discharge capacity but poorer cycling stability on the T-Oct samples, as compared to the Plate sample. For high energy applications that require stable operation at high voltages, replacing the

more reactive (012) surface with less reactive (001) or (104) surface is an effective strategy. This can be achieved by adjusting synthesis conditions that favor particles with (001) and/or (104) over (012) surface. Although the tradeoffs between cathode capacity and stability remains a challenge, our study demonstrates that surface engineering provides an additional avenue in material optimization.

Acknowledgements

We thank Drs. Jianhua Yan and Wang Hay Kan for experimental assistance, Drs. Hakim Iddir, Jason Croy and Juan Garcia at Argonne National Laboratory for fruitful discussions, Drs. Marca Doeff, Dennis Nordlund and Ryan Davis for the help with the XAS measurements carried out at SSRL. Use of the Stanford Synchrotron Radiation Lightsource, SLAC National Accelerator Laboratory, is supported by the U.S. Department of Energy, Office of Science, Office of Basic Energy Sciences under Contract No. DE-AC02-76SF00515. This work was supported by the Assistant Secretary for Energy Efficiency and Renewable Energy, Office of FreedomCAR and Vehicle Technologies of the U.S. Department of Energy under Contract No. DE-AC02-05CH11231.

References

1. Ding, Y.; Mu, D.; Wu, B.; Wang, R.; Zhao, Z.; Wu, F., Recent progresses on nickel-rich layered oxide positive electrode materials used in lithium-ion batteries for electric vehicles. *Appl. Energy* **2017,** *195*, 586-599.

2. Xu, J.; Lin, F.; Doeff, M. M.; Tong, W., A review of Ni-based layered oxides for rechargeable Li-ion batteries. *J. Mater. Chem. A* **2017,** *5* (3), 874-901.

3. Yoon, C. S.; Choi, M. H.; Lim, B. B.; Lee, E. J.; Sun, Y. K., Review-High-Capacity Li Ni1-xCox/2Mnx/2 O-2 (x=0.1, 0.05, 0) Cathodes for Next-Generation Li-Ion Battery. *J. Electrochem. Soc.* **2015,** *162* (14), A2483-A2489.

4. Schipper, F.; Erickson, E. M.; Erk, C.; Shin, J.-Y.; Chesneau, F. F.; Aurbach, D., Review—Recent Advances and Remaining Challenges for Lithium Ion Battery Cathodes: I. Nickel-Rich, LiNixCoyMnzO2. *J. Electrochem. Soc.* **2017,** *164* (1), A6220-A6228.

5. Konarov, A.; Myung, S. T.; Sun, Y. K., Cathode Materials for Future Electric Vehicles and Energy Storage Systems. *ACS Energy Lett.* **2017,** *2* (3), 703-708.

6. Liu, W.; Oh, P.; Liu, X.; Lee, M. J.; Cho, W.; Chae, S.; Kim, Y.; Cho, J., Nickel-Rich Layered Lithium Transition-Metal Oxide for High-Energy Lithium-Ion Batteries. *Angew. Chem. Int. Ed.* **2015,** *54* (15), 4440-4457.

7. Li, J.; Camardese, J.; Shunmugasundaram, R.; Glazier, S.; Lu, Z.; Dahn, J. R., Synthesis and Characterization of the Lithium-Rich Core–Shell Cathodes with Low Irreversible Capacity and Mitigated Voltage Fade. *Chem. Mater.* **2015,** *27* (9), 3366-3377.

8. Li, W.; Song, B.; Manthiram, A., High-voltage positive electrode materials for lithium-ion batteries. *Chem. Soc. Rev.* **2017,** *46* (10), 3006-3059.

9. Hu, E.; Wang, X.; Yu, X.; Yang, X.-Q., Probing the Complexities of Structural Changes in Layered Oxide Cathode Materials for Li-Ion Batteries during Fast Charge–Discharge Cycling and Heating. *Acc. Chem. Res.* **2018,** *51* (2), 290-298.

10. Tian, C.; Lin, F.; Doeff, M. M., Electrochemical Characteristics of Layered Transition Metal Oxide Cathode Materials for Lithium Ion Batteries: Surface, Bulk Behavior, and Thermal Properties. *Acc. Chem. Res.* **2017,** *51* (1), 89-96.

11. Lin, F.; Liu, Y.; Yu, X.; Cheng, L.; Singer, A.; Shpyrko, O. G.; Xin, H. L.; Tamura, N.; Tian, C.; Weng, T.-C.; Yang, X.-Q.; Meng, Y. S.; Nordlund, D.; Yang, W.; Doeff, M. M., Synchrotron X-ray Analytical Techniques for Studying Materials Electrochemistry in Rechargeable Batteries. *Chem. Rev.* **2017,** *117* (21), 13123-13186.

12. Sun, H.-H.; Manthiram, A., Impact of Microcrack Generation and Surface Degradation on a Nickel-Rich Layered Li[Ni0.9Co0.05Mn0.05]O2 Cathode for Lithium-Ion Batteries. *Chem. Mater.* **2017,** *29* (19), 8486-8493.

13. Manthiram, A.; Song, B.; Li, W., A perspective on nickel-rich layered oxide cathodes for lithium-ion batteries. *Energy Storage Materials* **2017,** *6*, 125-139.

14. Jung, S.-K.; Gwon, H.; Hong, J.; Park, K.-Y.; Seo, D.-H.; Kim, H.; Hyun, J.; Yang, W.; Kang, K., Understanding the Degradation Mechanisms of LiNi0.5Co0.2Mn0.3O2 Cathode Material in Lithium Ion Batteries. *Adv. Energy Mater.* **2014,** *4* (1), 1300787-n/a.

15. Zou, L.; Zhao, W.; Liu, Z.; Jia, H.; Zheng, J.; Wang, G.; Yang, Y.; Zhang, J.-G.; Wang, C., Revealing Cycling Rate-Dependent Structure Evolution in Ni-Rich Layered Cathode Materials. *ACS Energy Lett.* **2018,** *3* (10), 2433-2440.

16. Lin, F.; Markus, I. M.; Nordlund, D.; Weng, T.-C.; Asta, M. D.; Xin, H. L.; Doeff, M. M., Surface reconstruction and chemical evolution of stoichiometric layered cathode materials for lithium-ion batteries. *Nat. Commun.* **2014,** *5*, 3529.

17. Ryu, H.-H.; Park, K.-J.; Yoon, C. S.; Sun, Y.-K., Capacity Fading of Ni-Rich Li[NixCoyMn1−x−y]O2 ($0.6 \leqslant x \leqslant 0.95$) Cathodes for High-Energy-Density Lithium-Ion Batteries: Bulk or Surface Degradation? *Chem. Mater.* **2018,** *30* (3), 1155-1163.

18. Yan, P. F.; Zheng, J. M.; Gu, M.; Xiao, J.; Zhang, J. G.; Wang, C. M., Intragranular cracking as a critical barrier for high-voltage usage of layer-structured cathode for lithium-ion batteries. *Nat. Commun.* **2017,** *8*, 14101.

19. Huang, Q.; Ma, L.; Liu, A.; Ma, X.; Li, J.; Wang, J.; Dahn, J. R., The reactivity of charged positive Li1-n[NixMnyCoz]O2 electrodes with electrolyte at elevated temperatures using accelerating rate calorimetry. *J. Power Sources* **2018,** *390*, 78-86.

20. Fang, S.; Jackson, D.; Dreibelbis, M. L.; Kuech, T. F.; Hamers, R. J., Anode-originated SEI migration contributes to formation of cathode-electrolyte interphase layer. *J. Power Sources* **2018,** *373*, 184-192.

21. Li, J.; Downie, L. E.; Ma, L.; Qiu, W. D.; Dahn, J. R., Study of the Failure Mechanisms of LiNi0.8Mn0.1Co0.1O2 Cathode Material for Lithium Ion Batteries. *J. Electrochem. Soc.* **2015,** *162* (7), A1401-A1408.

22. Gilbert, J. A.; Shkrob, I. A.; Abraham, D. P., Transition Metal Dissolution, Ion Migration, Electrocatalytic Reduction and Capacity Loss in Lithium-Ion Full Cells. *J. Electrochem. Soc.* **2017,** *164* (2), A389-A399.

23. Wandt, J.; Freiberg, A.; Thomas, R.; Gorlin, Y.; Siebel, A.; Jung, R.; Gasteiger, H. A.; Tromp, M., Transition metal dissolution and deposition in Li-ion batteries investigated by operando X-ray absorption spectroscopy. *J. Mater. Chem. A* **2016,** *4* (47), 18300-18305.

24. Zheng, H.; Sun, Q.; Liu, G.; Song, X.; Battaglia, V. S., Correlation between dissolution behavior and electrochemical cycling performance for LiNi1/3Co1/3Mn1/3O2-based cells. *J. Power Sources* **2012,** *207*, 134-140.

25. Schwieters, T.; Evertz, M.; Fengler, A.; Börner, M.; Dagger, T.; Stenzel, Y.; Harte, P.; Winter, M.; Nowak, S., Visualizing elemental deposition patterns on carbonaceous anodes from lithium ion batteries: A laser ablation-inductively coupled plasma-mass spectrometry study on factors influencing the deposition of lithium, nickel, manganese and cobalt after dissolution and migration from the Li1[Ni1/3Mn1/3Co1/3]O2 and LiMn1.5 Ni0.5O4 cathode. *J. Power Sources* **2018,** *380*, 194-201.

26. Garcia, J. C.; Bareno, J.; Yan, J. H.; Chen, G. Y.; Hauser, A.; Croy, J. R.; Iddir, H., Surface Structure, Morphology, and Stability of Li(Ni1/3Mn1/3Co1/3)O-2 Cathode Material. *J. Phys. Chem. C* **2017,** *121* (15), 8290-8299.

27. Kramer, D.; Ceder, G., Tailoring the Morphology of LiCoO2: A First Principles Study. *Chem. Mater.* **2009,** *21* (16), 3799-3809.

28. Cho, E.; Seo, S.-W.; Min, K., Theoretical Prediction of Surface Stability and Morphology of LiNiO2 Cathode for Li Ion Batteries. *ACS Appl. Mater. Interfaces* **2017,** *9* (38), 33257-33266.

29. Liang, C.; Longo, R. C.; Kong, F.; Zhang, C.; Nie, Y.; Zheng, Y.; Cho, K., Ab initio Study on Surface Segregation and Anisotropy of Ni-rich LiNi1-2yCoyMnyO2 (NCM) ($y \leqslant 0.1$) Cathodes. *ACS Appl. Mater. Interfaces* **2018,** *10* (7), 6673-6680.

30. Sharifi-Asl, S.; Soto, F. A.; Nie, A. M.; Yuan, Y. F.; Asayesh-Ardakani, H.; Foroozan, T.; Yurkiv, V.; Song, B.; Mashayek, F.; Klie, R. F.; Amine, K.; Lu, J.; Balbuena, P. B.; Shahbazian-Yassar, R., Facet-Dependent Thermal Instability in LiCoO2. *Nano Lett.* **2017,** *17* (4), 2165-2171.

31. Yan, P. F.; Zheng, J. M.; Zheng, J. X.; Wang, Z. G.; Teng, G. F.; Kuppan, S.; Xiao, J.; Chen, G. Y.; Pan, F.; Zhang, J. G.; Wang, C. M., Ni and Co Segregations on Selective Surface Facets and Rational Design of Layered Lithium Transition-Metal Oxide Cathodes. *Adv. Energy Mater.* **2016,** *6* (9), 1502455.

32. Zhang, H. L.; Omenya, F.; Yan, P. F.; Luo, L. L.; Whittingham, M. S.; Wang, C. M.; Zhou, G. W., Rock-Salt Growth-Induced (003) Cracking in a Layered Positive Electrode for Li-Ion Batteries. *ACS Energy Lett.* **2017,** *2* (11), 2607-2615.

33. Chen, G. Y.; Hai, B.; Shukla, A. K.; Duncan, H., Impact of Initial Li Content on Kinetics and Stabilities of Layered Li1+x(Ni0.33Mn0.33Co0.33)(1-x)O-2. *J. Electrochem. Soc.* **2012,** *159* (9), A1543-A1550.

34. Wang, F.; Xiao, S.; Chang, Z.; Yang, Y.; Wu, Y., Nanoporous LiNi1/3Co1/3Mn1/3O2 as an ultra-fast charge cathode material for aqueous rechargeable lithium batteries. *Chem. Commun.* **2013,** *49* (80), 9209-9211.

35. Huang, Z.-D.; Liu, X.-M.; Oh, S.-W.; Zhang, B.; Ma, P.-C.; Kim, J.-K., Microscopically porous, interconnected single crystal LiNi1/3Co1/3Mn1/3O2 cathode material for Lithium ion batteries. *J. Mater. Chem.* **2011,** *21* (29), 10777-10784.

36. Choi, J.; Manthiram, A., Crystal chemistry and electrochemical characterization of layered LiNi0.5−yCo0.5−yMn2yO2 and LiCo0.5−yMn0.5−yNi2yO2 ($0 \leqslant 2y \leqslant 1$) cathodes. *J. Power Sources* **2006,** *162* (1), 667-672.

37. Lee, K.-S.; Myung, S.-T.; Amine, K.; Yashiro, H.; Sun, Y.-K., Structural and Electrochemical Properties of Layered $Li[Ni1-2x\ Co\ x\ Mn\ x\ ]O2\ (x=0.1-0.3)$ Positive Electrode Materials for Li-Ion Batteries. *J. Electrochem. Soc.* **2007,** *154* (10), A971-A977.

38. Xiao, J.; Chernova, N. A.; Whittingham, M. S., Influence of Manganese Content on the Performance of LiNi0.9−yMnyCo0.1O2 ($0.45 \leqslant y \leqslant 0.60$) as a Cathode Material for Li-Ion Batteries. *Chem. Mater.* **2010,** *22* (3), 1180-1185.

39. Min, K.; Kim, K.; Jung, C.; Seo, S.-W.; Song, Y. Y.; Lee, H. S.; Shin, J.; Cho, E., A comparative study of structural changes in lithium nickel cobalt manganese oxide as a function of Ni content during delithiation process. *J. Power Sources* **2016,** *315*, 111-119.

40. Sun, H.; Zhao, K., Electronic Structure and Comparative Properties of LiNixMnyCozO2 Cathode Materials. *J. Phys. Chem. C* **2017,** *121* (11), 6002-6010.

41. Yoon, C. S.; Park, K.-J.; Kim, U.-H.; Kang, K. H.; Ryu, H.-H.; Sun, Y.-K., High-Energy Ni-Rich Li[NixCoyMn1–x–y]O2 Cathodes via Compositional Partitioning for Next-Generation Electric Vehicles. *Chem. Mater.* **2017,** *29* (24), 10436-10445.

42. Kuppan, S.; Shukla, A. K.; Membreno, D.; Nordlund, D.; Chen, G., Revealing Anisotropic Spinel Formation on Pristine Li- and Mn-Rich Layered Oxide Surface and Its Impact on Cathode Performance. *Adv. Energy Mater.* **2017,** *7* (11), 1602010.

43. Lin, F.; Nordlund, D.; Markus, I. M.; Weng, T.-C.; Xin, H. L.; Doeff, M. M., Profiling the nanoscale gradient in stoichiometric layered cathode particles for lithium-ion batteries. *Energy Environ. Sci.* **2014,** *7* (9), 3077-3085.

44. Tian, C.; Nordlund, D.; Xin, H. L.; Xu, Y.; Liu, Y.; Sokaras, D.; Lin, F.; Doeff, M. M., Depth-Dependent Redox Behavior of LiNi0.6Mn0.2Co0.2O2. *J. Electrochem. Soc.* **2018,** *165* (3), A696-A704.

45. Liu, X.; Wang, D.; Liu, G.; Srinivasan, V.; Liu, Z.; Hussain, Z.; Yang, W., Distinct charge dynamics in battery electrodes revealed by in situ and operando soft X-ray spectroscopy. *Nat. Commun.* **2013,** *4*, 2568.

46. Weber, R.; Fell, C. R.; Dahn, J. R.; Hy, S., Operando X-ray Diffraction Study of Polycrystalline and Single-Crystal LixNi0.5Mn0.3Co0.2O2. *J. Electrochem. Soc.* **2017,** *164* (13), A2992-A2999.

Table 1. Synthesis conditions for NMC crystal samples

NMC Samples			Precursors	Flux/R ratio	T (ºC)	t (h)
Composition	**Morphology**	**Size (μm)**				
333 or 622	Oct	10	TM acetates/Li_2CO_3	CsCl/LiCl=1/4	900	12
532	T-Oct	10	TM acetates/Li_2CO_3	CsCl/4	850	12
811	T-Oct	10	TM nitrates/LiOH	CsCl/4	900	12
333 or 622	T-Oct	1	TM nitrates/LiOH	CsCl/4	900	12
532	T-Oct	1	TM nitrates/ Li_2CO_3	CsCl/4	900	12
811	T-Oct	1	TM nitrates/LiOH	KCl/4	850	10
532	Poly	1	TM nitrates/ $LiNO_3$	CsCl/2	850	8
333 or 532	T-Oct	0.5	TM nitrates/ $LiNO_3$	KCl/4	850	12
333, 532 or 622	T-Oct	0.1	TM nitrates/LiOH	KCl/48	850	12
811	T-Oct	0.1	TM nitrates/LiOH	KCl/48	880	10
333	Plate	0.1	TM hydroxides/LiOH	-	850	10
622	Plate	0.1	TM hydroxides/LiOH	-	800	10

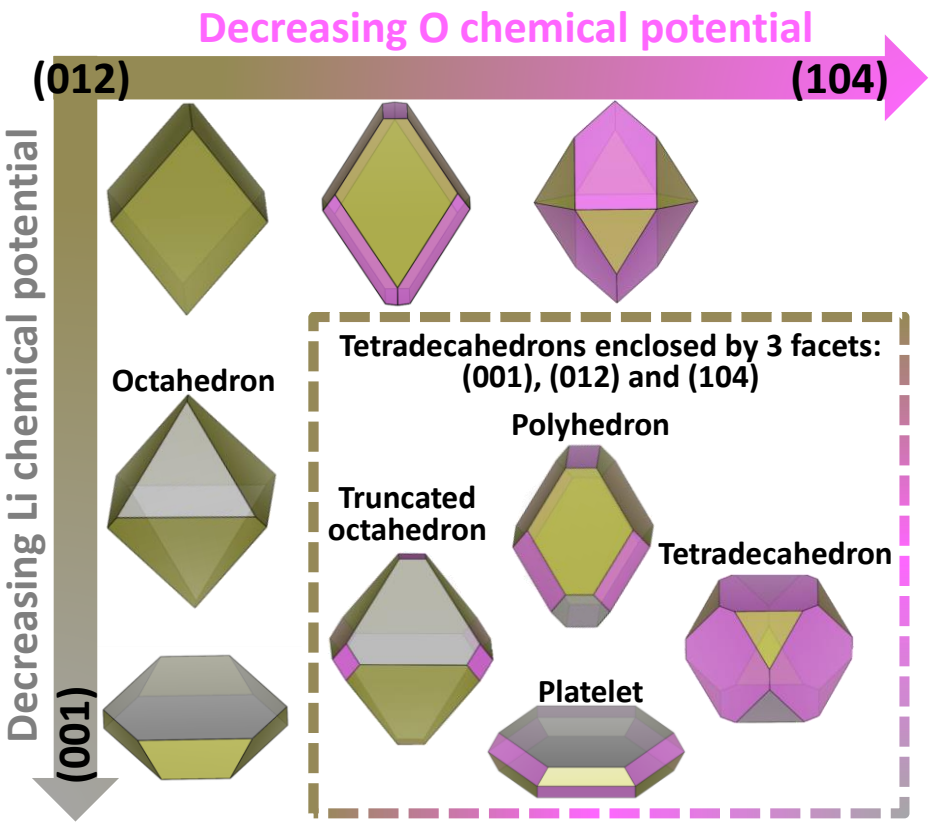

Figure 1. Schematics showing evolution of crystal shape as a function of O and Li chemical potentials and their influence on the presence of (012), (001) and (104) facets on the surface. Inset in the dashed line box shows various tetradecahedrons enclosed by the three facets.

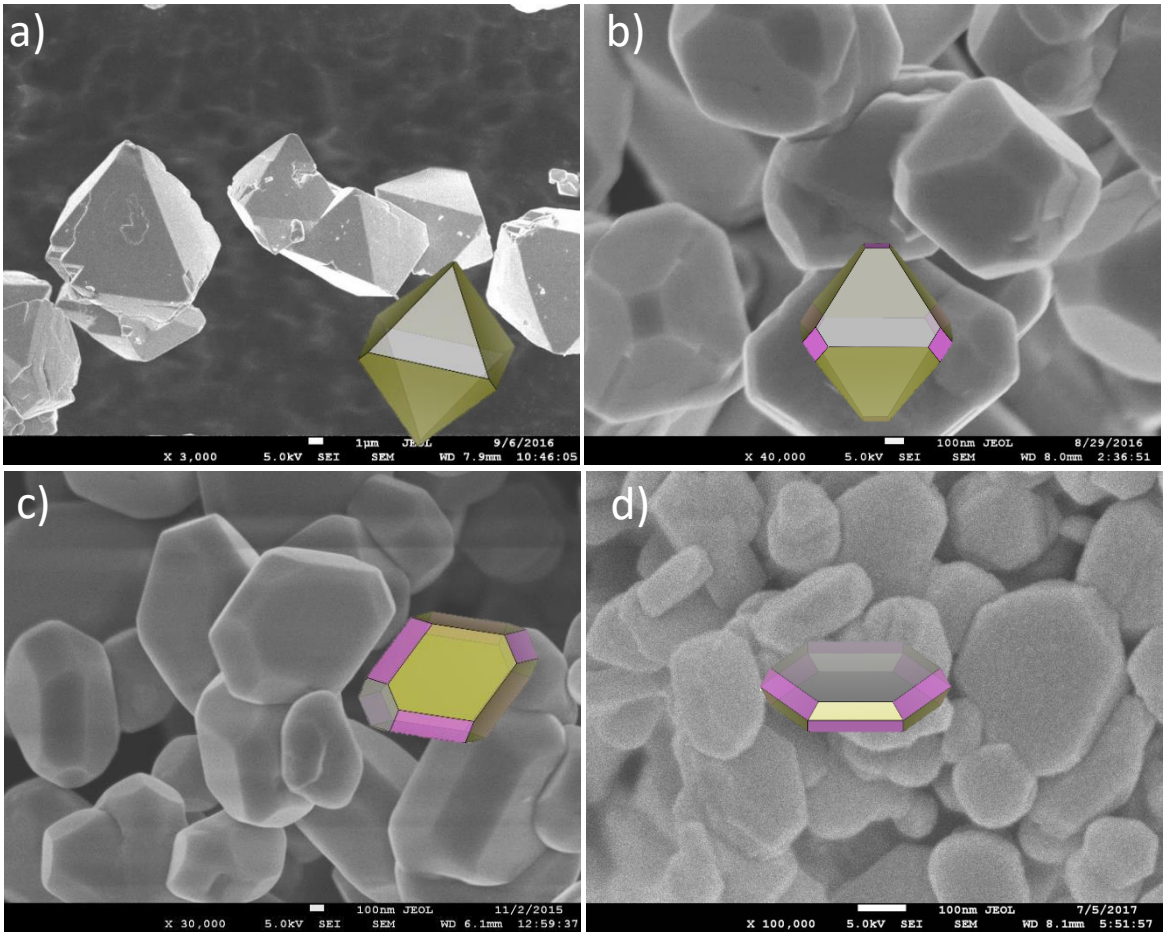

Figure 2. SEM images of NMC crystal samples with four differet morphologies: a) octahedron-shaped (Oct), b) truncated-octahedron-shaped (T-Oct), c) polyhedron-shaped (Poly) and d) platelet-shaped (Plate).

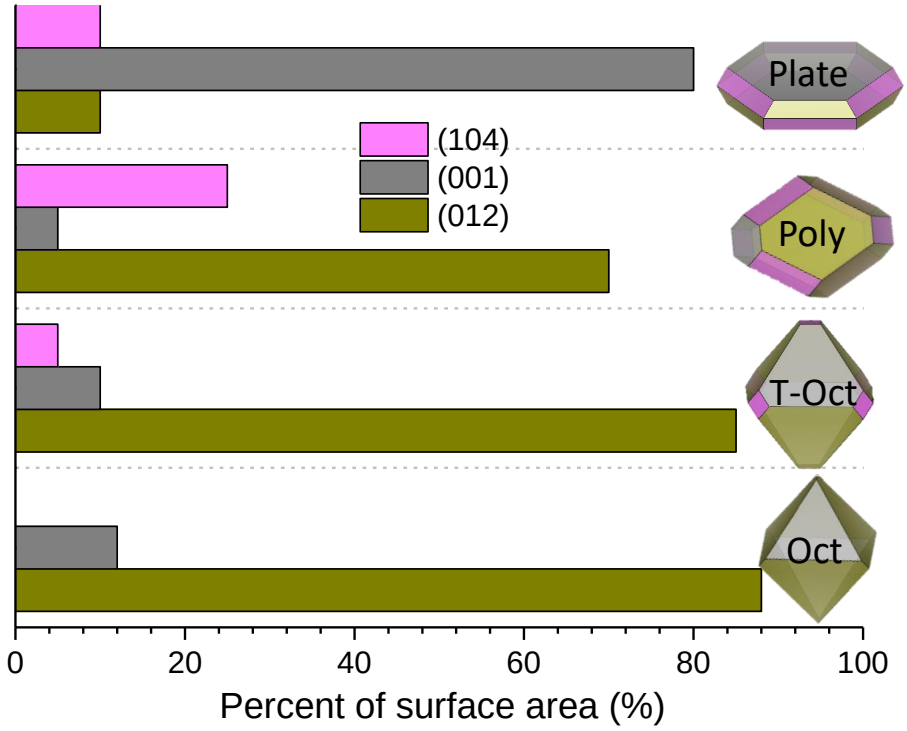

Figure 3. Percentage of each crystal facet appearing on the surface of synthesized NMC crystal samples.

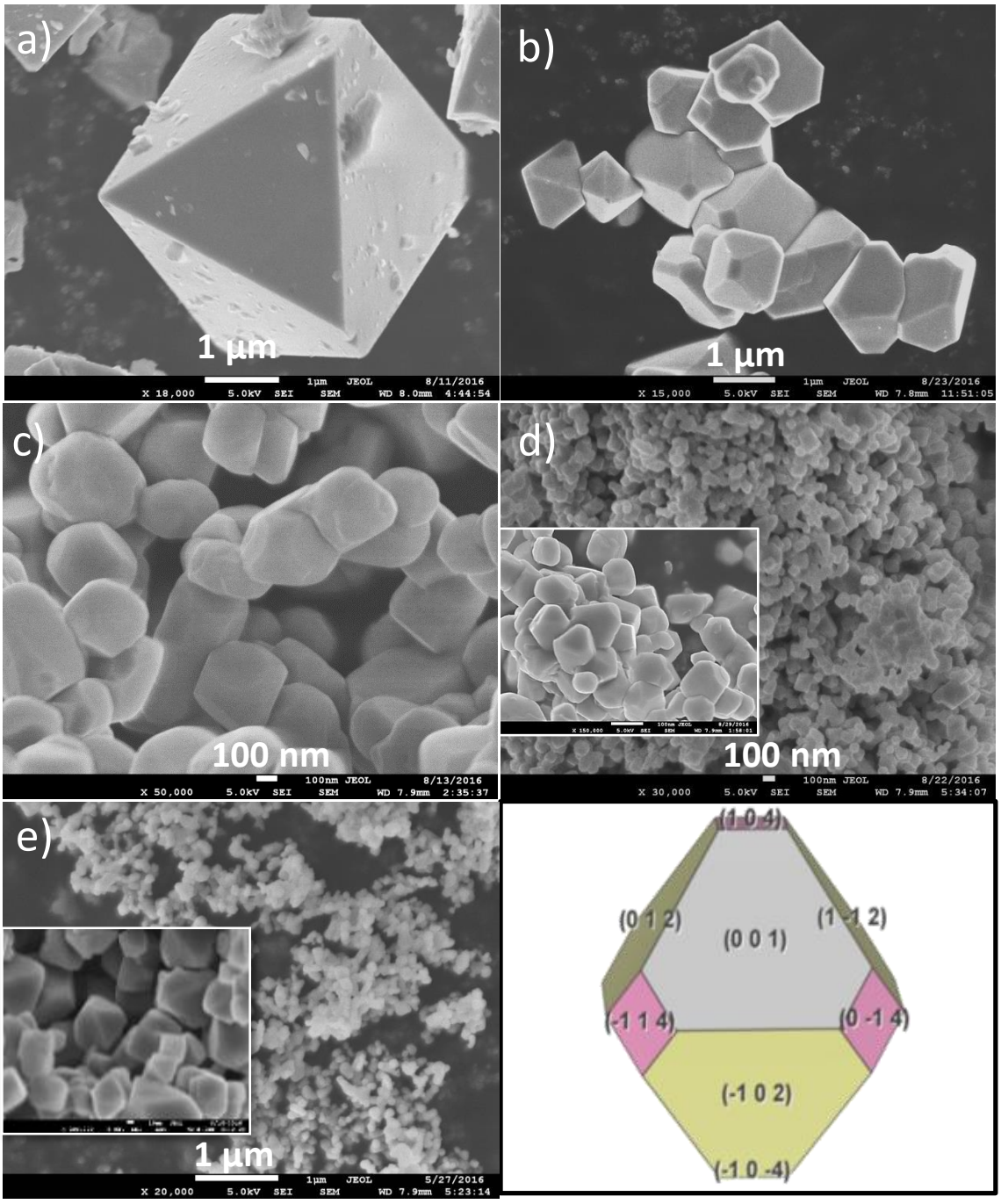

Figure 4. SEM images of T-Oct NMC532 with different sizes: a) 10 µm, b) 1 µm, c) 0.5 µm, d) 0.1 µm, e) 50 nm and f) facet distribution on T-Oct surface.

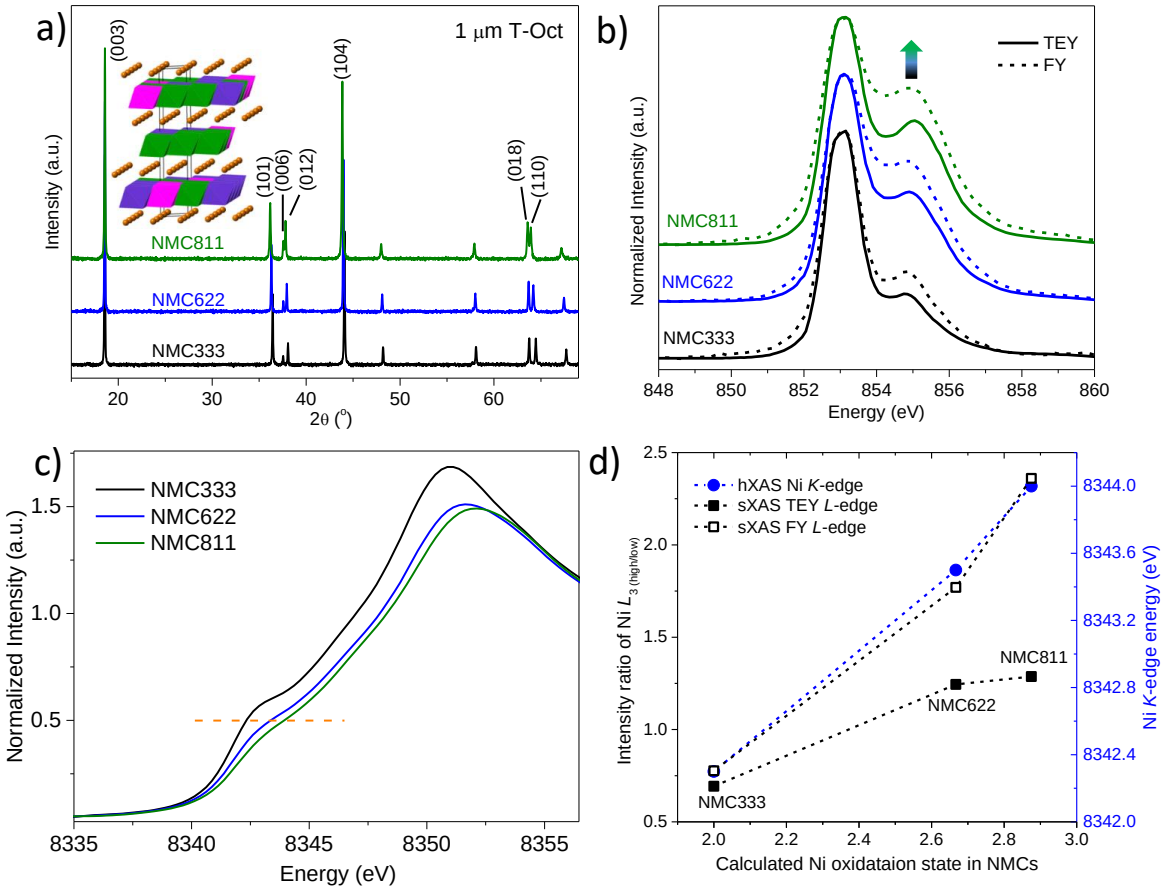

Figure 5. a) XRD patterns, b) Ni L_3-edge soft XAS spectra collected in TEY and FY modes, c) Ni *K*-edge hard XAS spectra, and d) changes in the ratio of high/low L_3-edge peaks and *K*-edge energy positions as a function of calculated Ni oxidation state in 1 μm T-Oct NMC333, NMC622 and NMC811 samples.

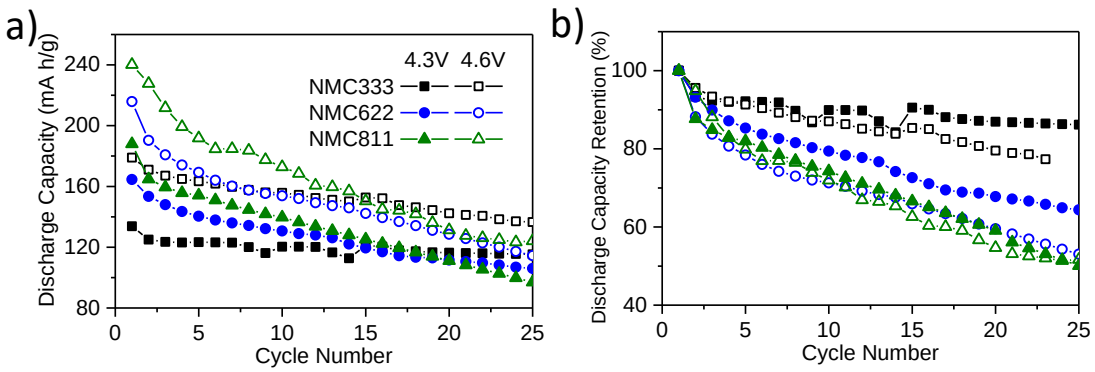

Figure 6. The impact of Ni content on electrochemical performance of 1 µm sized T-Oct NMC333, NMC622 and NMC811: a) discharge capacity as a function of cycle number and b) discharge capacity retention.

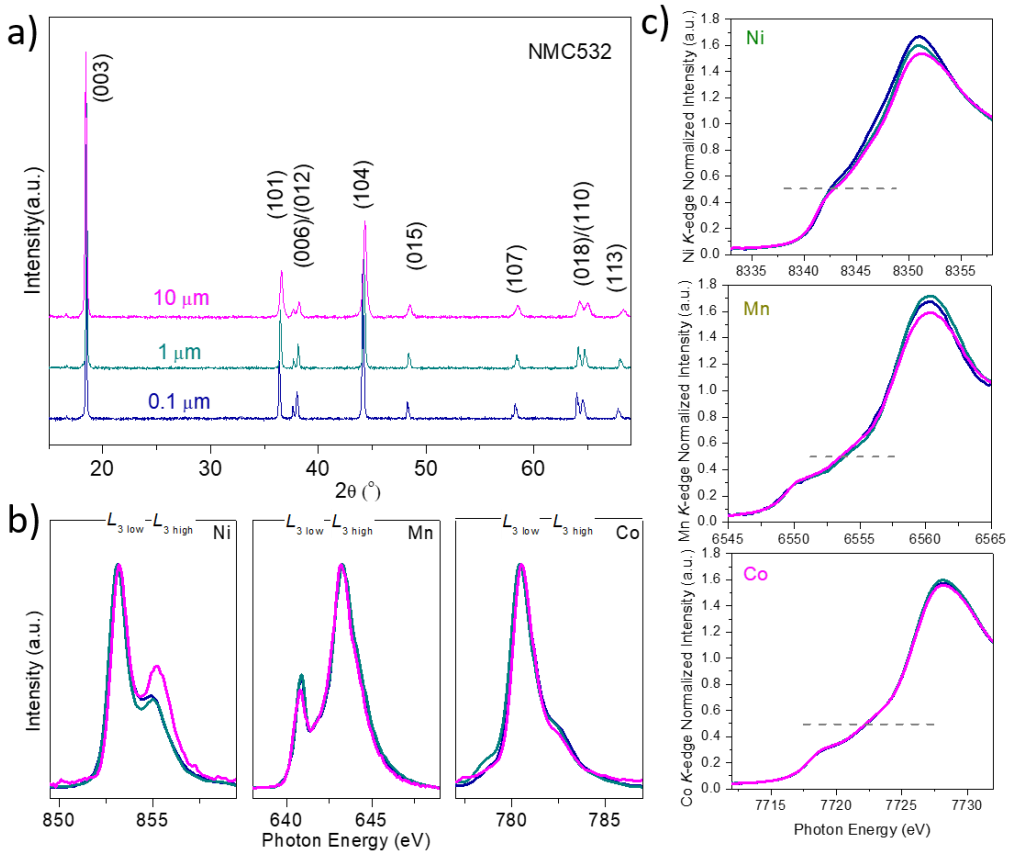

Figure 7. a) XRD patterns, b) Ni, Mn and Co soft XAS L_3-edge spectra in TEY mode, and c) *K*-edge XANES spectra of pristine NMC532 T-Oct with a particle size of 10 μm, 1 μm and 0.1 μm.

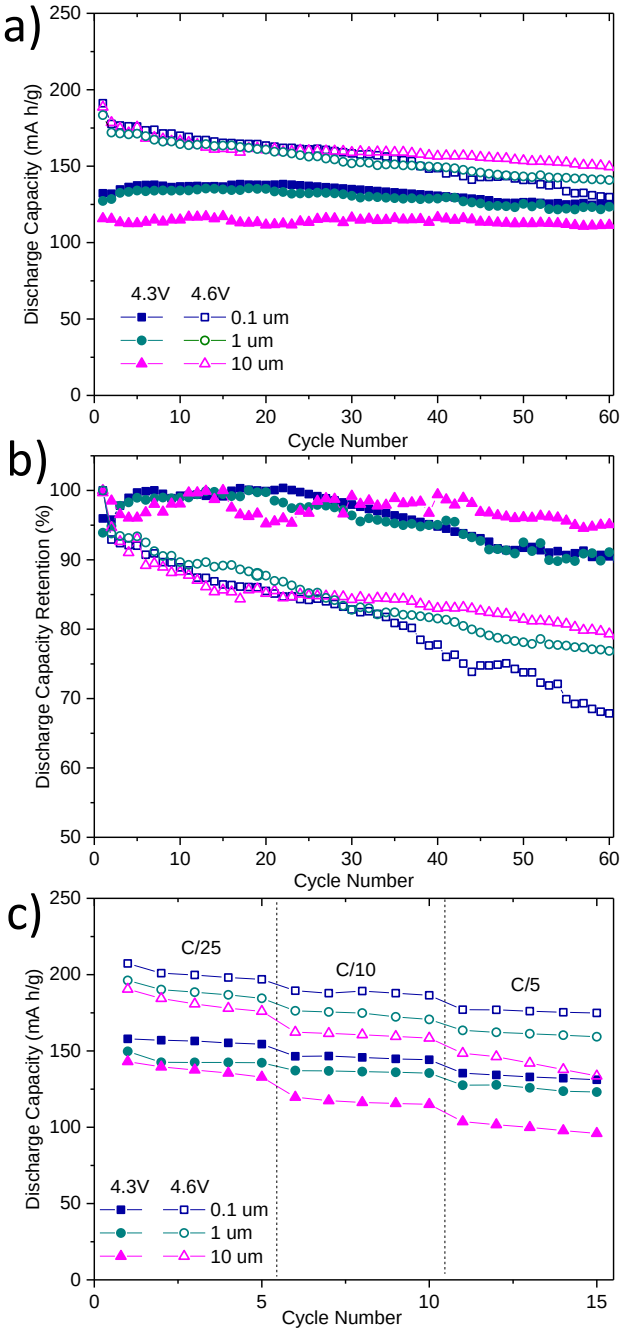

Figure 8. a) Discharge capacity, b) capacity retention at C/10 and c) rate capability of NMC532 crystal samples cycled between 3.0-4.3 V (solid) and 3.0-4.6 V (hollow), respectively.

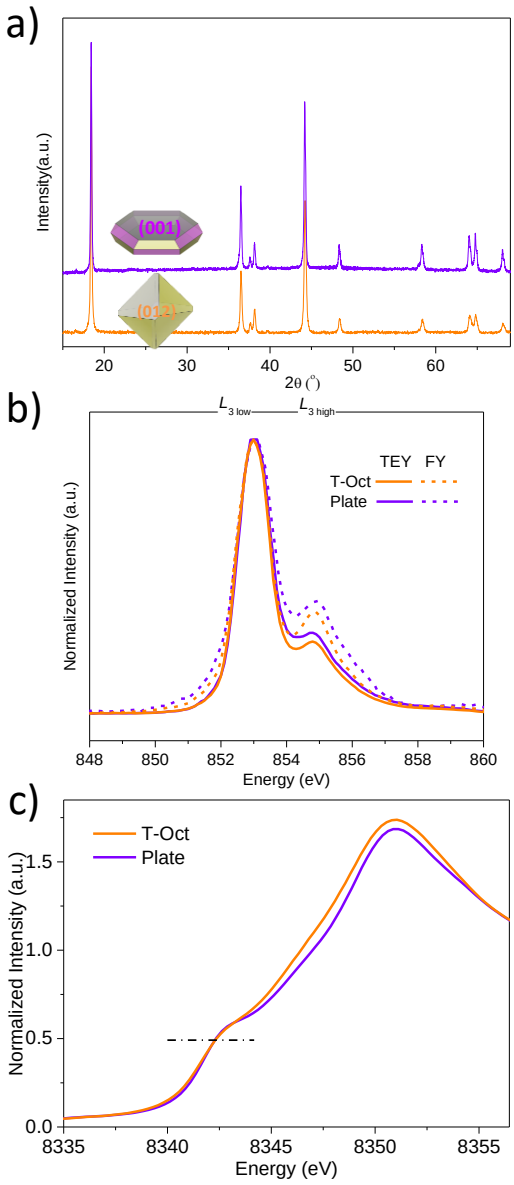

Figure 9. a) XRD patterns, b) sXAS Ni L_3-edge spectra in TEY and FY modes and c) hXAS Ni *K*-edge spectra of 0.1 μm NMC333 samples, with T-Oct dominated by (012) surface and Plate dominated by (001) surface.

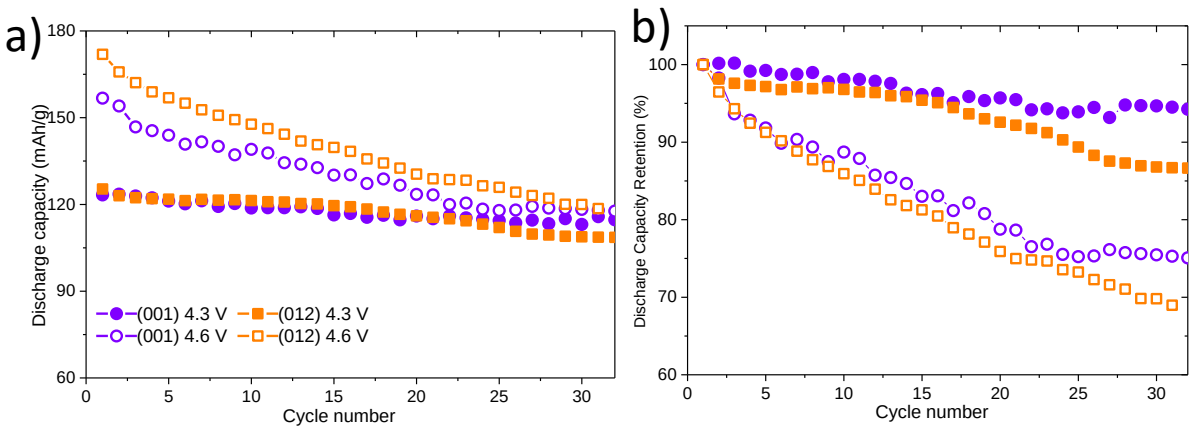

Figure 10. a) Cycling stability at C/10 and b) discharge capacity retention when cycled between 3.0-4.3 V (solid) and 3.0-4.6 V (hollow).

Table of Contents

Particle surface design is shown to be essential in optimizing the performance and stability of NMC-type LIB cathode materials.